IJMMM International Journal of Minerals, Metallurgy and Materials 矿物冶金与材料学报（英文版）

Hybrid $CoMoO_3$/$CoMoO_4$ nanorods for enhanced lithium-ion battery performance

Lijia Wan, Tingting Zhang, Ran Sun, Chunlai Huang, Ting Lu, Junping Hu, and Likun Pan

Cite this article as:
Lijia Wan, Tingting Zhang, Ran Sun, Chunlai Huang, Ting Lu, Junping Hu, and Likun Pan, Hybrid $CoMoO_3$/$CoMoO_4$ nanorods for enhanced lithium-ion battery performance, *Int. J. Miner. Metall. Mater.*, 32(2025), No. 8, pp. 1997-2006. https://doi.org/10.1007/s12613-024-3051-0

INTERNATIONAL JOURNAL OF
Minerals, Metallurgy and Materials

Volume 32, Number 8, August 2025
Page 1997

Research Article https://doi.org/10.1007/s12613-024-3051-0

Hybrid $CoMoO_3/CoMoO_4$ nanorods for enhanced lithium-ion battery performance

Lijia Wan[1,2)✉], *Tingting Zhang*[1)], *Ran Sun*[1)], *Chunlai Huang*[1)], *Ting Lu*[2)], *Junping Hu*[1)], *and Likun Pan*[2)✉]

1) Nanchang Key Laboratory of Photoelectric Conversion and Energy Storage Materials, Nanchang Institute of Technology, Nanchang 330099, China
2) Shanghai Key Laboratory of Magnetic Resonance, School of Physics and Electronic Science, East China Normal University, Shanghai 200241, China
(Received: 5 October 2024; revised: 20 November 2024; accepted: 21 November 2024)

Abstract: Electrode materials that rely on conversion reactions for lithium-ion batteries (LIBs) possess high energy densities. However, a key issue in their design is bolstering their stability and minimizing volume variations during lithiation and delithiation. Herein, an effective strategy was devised to fulfill the fully reversible conversion reaction for lithium storage in $CoMoO_4$ through the hybridization of $CoMoO_3$. $CoMoO_3/CoMoO_4$ with a nanorod structure was synthesized via one-step annealing treatment after a solvothermal process. In such a structure, the $CoMoO_3/CoMoO_4$ nanorod can considerably boost mechanical robustness and offer ample space to counteract volume fluctuations throughout successive cycles owing to the cooperative interaction between $CoMoO_3$ and $CoMoO_4$. $CoMoO_3/CoMoO_4$ exhibited superior lithium-storage capacity (919.6 mAh/g at 0.1 A/g after 200 cycles) and cycling stability (683.4 mAh/g at 1 A/g after 600 cycles). $CoMoO_3/CoMoO_4$ showed a high potential as an anode material for LIBs.

Keywords: anode; $CoMoO_3/CoMoO_4$; nanorod structure; hybrid material; electrode materials; conversion reaction-type; lithium-ion batteries

1. Introduction

Transition-metal oxides accumulate lithium through conversion reactions, and they are reduced to metallic nanocrystals within a Li_2O matrix during the lithiation phase and re-oxidized to their original form during delithiation [1–5]. In addition, some transitional-metal oxides further accommodate lithium via alloying reactions after the formation of metallic nanocrystals, which provides extra capacity [6–10]. As a result, electrode materials based on metal oxides typically have theoretical specific capacities ranging from 600 to 1000 mAh/g, which surpass those of traditional graphite by a factor of 1.5–3. Moreover, bimetal oxides demonstrate better performance than monometal oxides and are thus well documented as substitutes for anodes with elevated capacities for lithium-ion batteries (LIBs) [11–13].

Among various bimetal oxides, $CoMoO_4$ is a prospective electrode for LIBs, and it is characterized by its theoretical capacity (980 mAh/g) and advantageous properties, including high conductivity and a range of oxidation states from molybdenum [14–19]. However, this material faces challenges, such as its sluggish reaction kinetics and poor cycling stability, which are often attributed to large volume changes and the configuration of a fragile solid–electrolyte interphase (SEI) layer.

The exceptional properties of nanostructure materials include swift migration channels for electrons and lithium ions, a broad interface that enables the interaction of the electrode with the electrolyte, paired with superior pliability and durability to manage the strain resulting from Li^+ insertion/extraction. Therefore, the above advantages make nanostructuring a powerful strategy for addressing the aforementioned challenges for $CoMoO_4$. Yu *et al.* [15] reported a hierarchically porous three-dimensional $CoMoO_4$ electrode that delivers a specific capacity of 894 mAh/g after 100 cycles. Porous $CoMoO_4$ nanorod reported by Wang *et al.* [20] delivered 603 mAh/g after 300 cycles at 0.4 A/g. They demonstrated exceptional lithium-storage performance after the design and fabrication of $CoMoO_4$ with various nanostructures. The introduction of carbon clamping shell layers is another strategy for preventing severe capacity fading, particularly at high current [21–23]. Furthermore, the large surface area of the modified anode materials can increase the number of ion storage sites and promote the penetration of the electrolyte, which enhances the specific capacity and the rate of ion transport [24]. As evidenced by researches [25–28], the association of $CoMoO_4$ with carbon materials realized improved electrochemical performance over pure $CoMoO_4$. However, carbon coating is often tedious and may lower the tap density or initial Coulombic efficiency [29].

A reported novel strategy introduces highly active nanosized Co-based oxides to stabilize structured electrodes and promote reversible insertion and extraction reactions in an atomically homogeneous manner [30–35]. Thus, seeking suitable Co-based oxide to decorate $CoMoO_4$ should be a powerful strategy to advance lithium-storage capacity, but

✉ Corresponding authors: Lijia Wan E-mail: wlj2090jx@163.com; Likun Pan E-mail: lkpan@phy.ecnu.edu.cn

such a task remains highly challenging. Wang *et al*. [30] reported a fully reversible $MoO_3/CoMoO_4$ was achieved through the introduction of Co-based oxide into $CoMoO_4$. In addition, valence-rich Mo (IV, V) oxides are more active than single-valence Mo (VI) oxides due to the altered charge distribution at the material interface [36–39]. Therefore, the introduction of $CoMoO_3$ into $CoMoO_4$ is deemed an effective means to realizing the conversion reaction of $CoMoO_4 + 8Li^+ + 8e^- \rightleftharpoons Mo + Co + 4Li_2O$ due to the combined advantages of the constructed $CoMoO_3$–$CoMoO_4$ hybrid. Moreover, *in-situ* formation of Co nanoclusters from $CoMoO_3$ and $CoMoO_4$ effectively curbs the aggregation of Mo nanocrystals and cushions the stress resulting from volume changes during the cycling process, which improves the capacity retention and cycling stability of the $CoMoO_3/CoMoO_4$ electrode.

Herein, hybrid $CoMoO_3/CoMoO_4$ nanorods were successfully synthesized via a straightforward two-step synthesis procedure, which included a solvohydrothermal reaction followed by a high-temperature annealing treatment. $CoMoO_3/CoMoO_4$ delivered a specific capacity of 919.6 mAh/g after 200 cycles at 0.1 A/g and 683.4 mAh/g after 600 cycles at 1 A/g and displayed an exceptional lithium-storage performance originating from the unique $CoMoO_3/CoMoO_4$ architecture and synergistic action. This work presents a novel strategy to boost the high-performance lithium storage of bimetal oxides and potentially offers considerable advancement in the field of energy storage materials.

2. Experimental

The fabrication process of $CoMoO_4$ (CMO-1) and $CoMoO_3/CoMoO_4$ (CMO-2) both involved the solvothermal reaction and annealing treatment. First, 1.1420 g $CoCl_2·6H_2O$ was dissolved in 60 mL triethylene glycol via magnetic stirring for 0.5 h, which resulted in a purple solution. Second, 1.1614 g Na_2MoO_4 was added to 10 mL deionized water and sonicated to create a transparent solution. Third, this solution was blended with the purple solution under magnetic stirring for 0.5 h. The solution color turned blue-violet and was deemed solution C. Then, solution C was placed in a Teflon-lined autoclave, maintained for 12 h at 120°C, and allowed to cool naturally. The violet precursor was retrieved through centrifugation and cleaned with ethanol to remove impurities before being dried at 60°C overnight. CMO-1 and CMO-2 products were achieved through thermal treatment of the violet precursors at 600 and 650°C for 1 h under N_2 atmosphere at a consistent heating rate of 2°C/min.

The comprehensive material assessments and explanation of electrochemical tests were shown in Supplementary Information.

3. Results and discussion

3.1. Results

The fabrication of CMO-1 and CMO-2 involved a solvothermal synthesis, followed by an annealing step. Thermogravimetric (TG) analysis was performed to ascertain the optimal annealing temperature of the precursor (Fig. S1). The TG curve indicated that annealing should be conducted at temperatures between 600 and 800°C, where a clear weight reduction was observed. X-ray diffraction (XRD) measurements were carried out to measure the crystal phase and structure of CMO-1 and CMO-2. As displayed in Fig. 1(a), for CMO-1, the typical peaks located at 23.32°, 26.56°, 27.38°, 28.70°, 32.25°, 33.79°, and 38.95° corresponded to the (021), (002), ($\bar{1}$12), ($\bar{3}$11), ($\bar{1}$31), ($\bar{2}$22), and (040) planes of $CoMoO_4$ (PDF#21-0868) [15,20,25,39], respectively, which imply that $CoMoO_4$ was successfully obtained via annealing after a hydrothermal process. For CMO-2, other than the several characteristic peaks of $CoMoO_4$ observed in CMO-1, the peak marked * at 19.7° was indicative of the ($\bar{2}$01) plane of $CoMoO_4$. Furthermore, the distinct peaks at 18.05°, 25.67°, 30.68°, 35.97°, 37.10°, 45.63°, and 49.24° corresponded to the (002), (102), (110), (200), (004), (203), and (114) planes of $CoMoO_3$ (PDF#21-0869) [40–41]. For a more in-depth analysis of the structure, Raman spectral analysis was further conducted. As shown in Fig. 1(b), the bands observed at 333, 365, 803, 869, and 933 cm^{-1} represent the stretching vibrations of Co–O–Mo in $CoMoO_4$ or $CoMoO_3$ [20,42–45]. To determine the composition of CMO-2, X-ray photoelectron spectroscopy (XPS) survey was conducted to analyze the sample. For the Co 2p XPS spectrum, two prominent peaks at 780.4 and 796.8 eV (Fig. 1(c)) corresponded to the Co $2p_{1/2}$ and Co $2p_{3/2}$ energy levels, respectively. In addition, the satellite peaks near 803.1 and 786.9 eV were associated with the shakeup-type peaks of the Co $2p_{1/2}$ and Co $2p_{3/2}$ edge, respectively, which is characteristic of the high-binding-energy Co side [20,46–48]. For the Mo 3d spectrum (Fig. 1(d)), the intense peak at 235.08 eV was attributed to Mo $3d_{3/2}$, and the strong peak at 232.0 eV and the faint peak at 229.9 eV corresponded to Mo $3d_{5/2}$, which signified the presence of Mo^{6+} and Mo^{4+} oxidation states [46–47,49–50]. Fig. 1(e) and (f) displays the N_2 adsorption–desorption isotherms and pore size distribution curves for CMO-1 and CMO-2, and Table S1 provides the corresponding specific surface area and mean pore diameter. CMO-2 exhibited higher specific surface area of 14.81 m^2/g than CMO-1 (10.97 m^2/g). The elevated surface area can offer more active sites for Li^+ storage. Notably, the pore sizes of the CMO-1 and CMO-2 were predominantly within that of mesopores (Fig. 1(f)), suggesting their potential for enhancing ion transport [30].

The morphological examination via field-emission scanning electron microscopy (FESEM) in Fig. 2(a)–(c) revealed that the precursor, CMO-1, and CMO-2 had a nanorod form. These nanorods interconnected and formed a network that enhanced ion transport. Further, the transmission electron microscopy (TEM) images of CMO-2 (Fig. 2(d) and (e)) revealed nanorods that were several micrometers in length, 300 nm wide, and 100 nm tall. The high-resolution TEM (HRTEM) images displayed an interplanar distance of

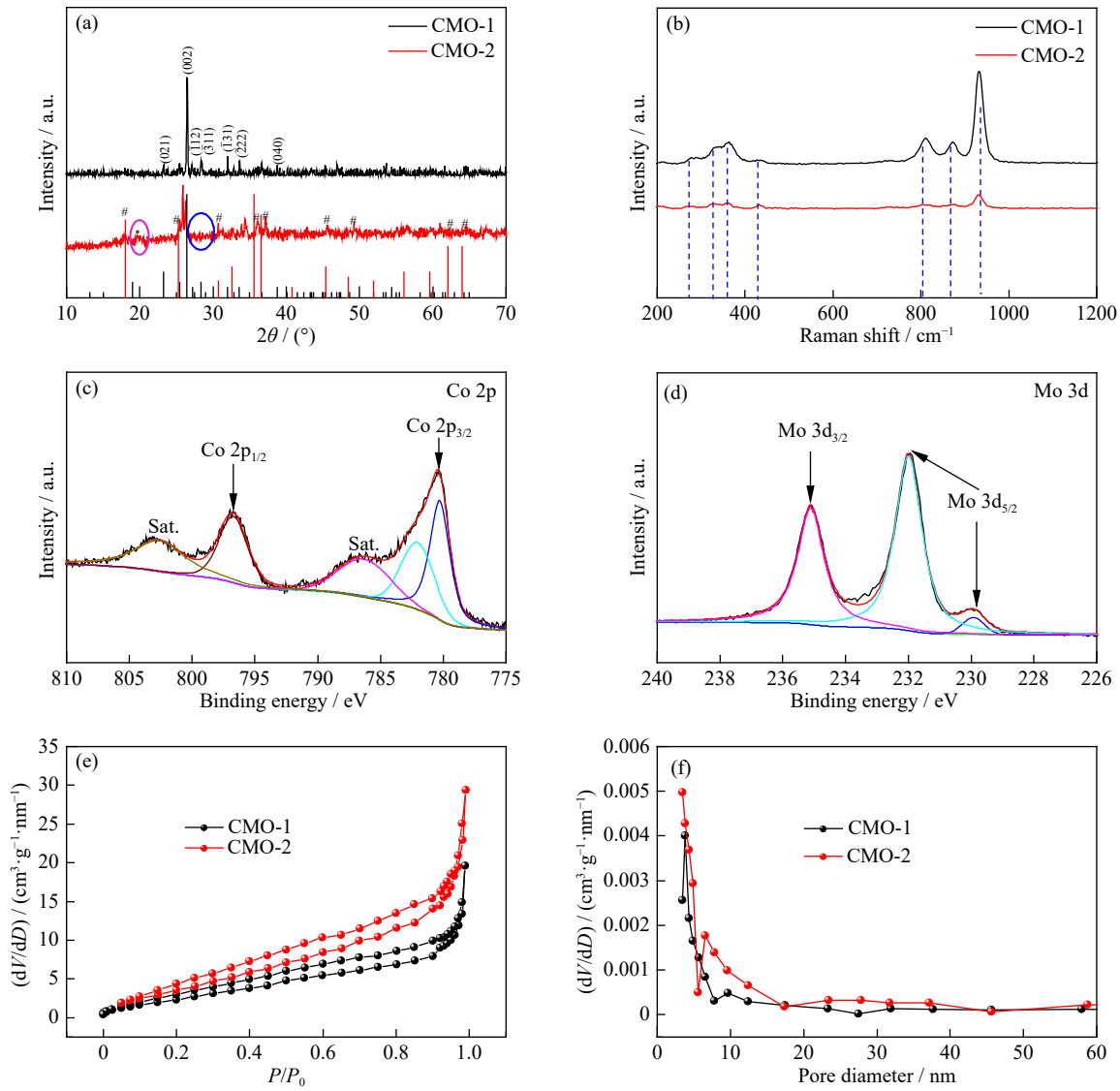

Fig. 1. (a) XRD and (b) Raman spectra of CMO-1 and CMO-2, (c) Co 2p and (d) Mo 3d XPS spectra of CMO-2, and (e) N_2 adsorption–desorption hysteresis loops and (f) their matching pore size distribution plots for CMO-1 and CMO-2.

0.44 nm, which corresponded to the $(\bar{2}01)$ plane of $CoMoO_4$, as shown in Fig. 2(f)–(i). Distances of 0.34 and 0.49 nm were associated with the (102) and (002) planes of $CoMoO_3$, respectively [30,35]. Moreover, the elemental mappings in Fig. 2(j)–(m) illustrate the even distribution of Co, Mo, and O within the samples. All the above results demonstrate the successful synthesis of the $CoMoO_3/CoMoO_4$ structure.

The lithium-storage performances of CMO-1 and CMO-2 as the anode material for LIBs were evaluated. Fig. 3(a) and (b) presents the cyclic voltammetry (CV) curves of the initial three cycles for CMO-1 and CMO-2 at 0.2 mV/s, respectively. For CMO-1, the initial cathodic process exhibited two reduction peaks at 0.30 and 0.12 V, which signifies the formation of metallic Co and Mo, respectively, solid electrolyte interphase film, and a peak at 1.21 V indicating Li_2O formation [15,44,51]. After the initial cycle, the reduction peaks at 1.52 and 0.62 V were ascribed to the reversible reduction reaction: $CoMoO_4 + 8Li^+ + 8e^- \rightleftharpoons Mo + Co + 4Li_2O$. During the anodic scans, two oxidation peaks of 1.44 and 1.84 V were detected, which signifies the oxidation reactions of Co and Mo. At 1.44 V, the peak implied the advancement from Mo^0 to Mo^{4+}, and that at 1.80 V was indicative of the change from Co to Co^{2+} and the further change from Mo^{4+} to Mo^{6+}. For CMO-1, the peak at 1.21 V denoted the formation of Li_2O, which was reversible but with a low intensity. For CMO-2, during the initial cathodic process, the 0.45 V reduction peak was linked to the intercalation of Li^+ into $CoMoO_4$, which resulted in the generation of metallic Co and Mo along with the formatting of SEI films. Meanwhile, the peak at 1.26 V indicated Li_2O formation. After the initial cycle, new peaks identified at approximately 0.62 and 1.26 V were linked to the reversible lithium uptake by $CoMoO_3$ and $CoMoO_4$, respectively. The identification of these new peaks indicates that the contribution of $CoMoO_3$ to the lithium-storage performance is important and should not be overlooked. In anodic scans, a prominent oxidation peak (1.44 V) along with a less intense peak (1.80 V) was observed, and it corresponded to the lithium reversible desertion occurring in $CoMoO_3$ and $CoMoO_4$. The peak at 1.44 V shifted right and intensified, and the peak at 1.80 V weakened due to the increased levels

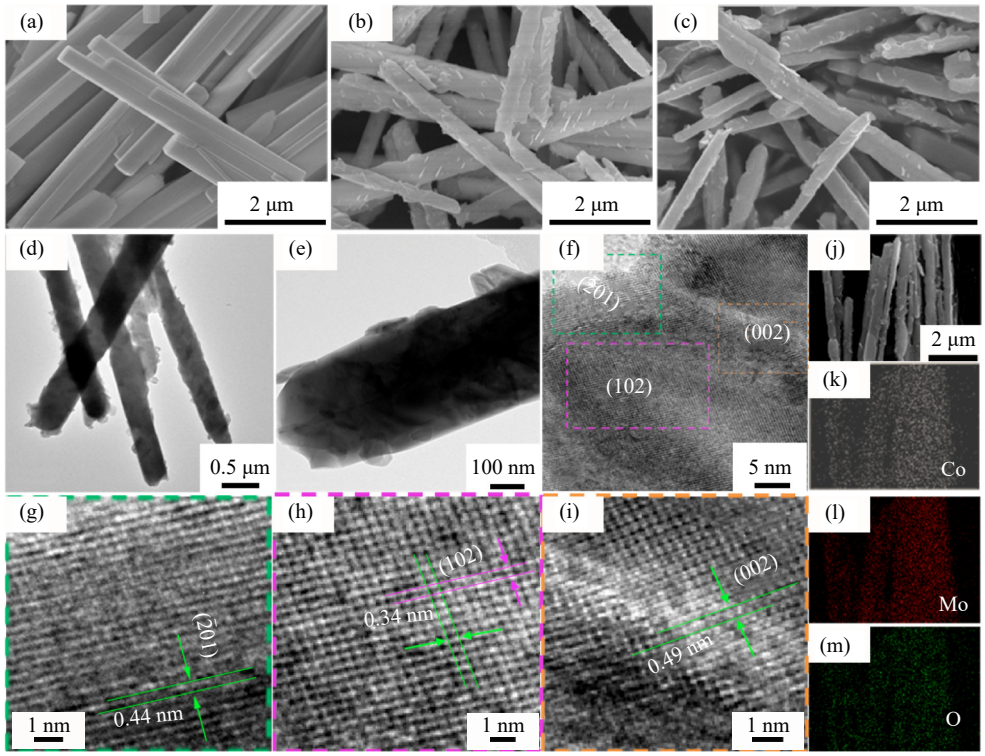

Fig. 2. FESEM images of (a) precursor, (b) CMO-1, and (c) CMO-2; (d, e) TEM images at different magnifications, (f–i) HRTEM images, and (j) enlarged FESEM image and (k–m) corresponding elemental mappings of CMO-2.

of the Co (II) and Mo (IV) components in the composite upon oxidation process and polarization. The peak at 1.21 V corresponding to Li_2O can be made fully reversible and shifted to 1.26 V after the first cycle, which should stem from the integrated effect of $CoMoO_3$ and $CoMoO_4$. Furthermore, the CV curves for CMO-2 exhibited a strong overlap after the initial cycle, which also demonstrates its enduring stability. The large specific surface area of CMO-2 promoted lithium insertion/extraction by providing more active sites for lithium ions, which is crucial for the enhanced rate capability and cycling stability of the anode material. The increased surface area allowed for more efficient contact between the electrode material and the electrolyte, which improved its electrochemical performance.

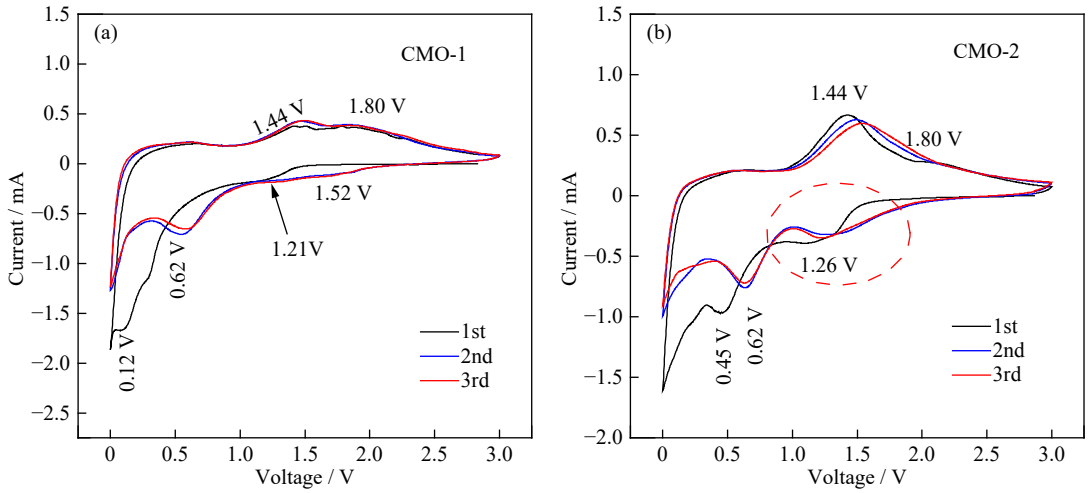

Fig. 3. CV curves of (a) CMO-1 and (b) CMO-2 at 0.2 mV/s.

Fig. 4(a) and (b) presents the galvanostatic discharge/charge curves at 0.1 A/g for CMO-1 and CMO-2, spanning from 0.001 to 3.0 V. Upon first discharge, CMO-1 displayed a clear peak at 1.80 V and a prolonged voltage flat spot at 0.5 V, which matched its CV curve. For CMO-2, the initial discharge curve was split into two regions at 1.5 V. In the region above 1.5 V, the capacity was an outcome of Li^+ insertion into $CoMoO_4$ formatting $CoMoO_3$, which was responsible for the 147.1 and 87.3 mAh/g capacities of CMO-1 and CMO-2, respectively. The lower capacity of CMO-2 was due to its composition of $CoMoO_4$ and $CoMoO_3$. When the voltage dropped below 1.5 V, a conversion reaction occurred, which was attributed to the transformation of Li_xMoO_3 and Li^+ into Mo and Li_2O, yielding 1021.1 and 1034.7 mAh/g for

CMO-1 and CMO-2, respectively. The initial cycle capacity fade was ascribed to the formation of Li_2O and SEI films and associated side reactions. CMO-2 exhibited well-aligned discharge/charge profiles and minimal capacity loss after the first cycle, and these findings signify its better cyclability compared with CMO-1. Such outcomes were attributed to the synergistic interaction between $CoMoO_3$ and $CoMoO_4$. Accordingly, the Coulombic efficiency of CMO-2 experienced a sharp increase, starting at 75.57% in the first cycle, and the value reached ~96.13% by the second cycle and remained above 98% beyond 200 cycles. Although the initial Coulombic efficiency of CMO-1 (84.24%) was higher than that of CMO-2 (75.57%), the Coulombic efficiency of CMO-2 was 93.43% in the second cycle, and it increased to 96.49% until the 5th cycle and remained above 98% after 200 cycles. The results demonstrate that the introduction of $CoMoO_3$ into $CoMoO_4$ can promote the fully reversible conversion of $CoMoO_4$ for LIBs.

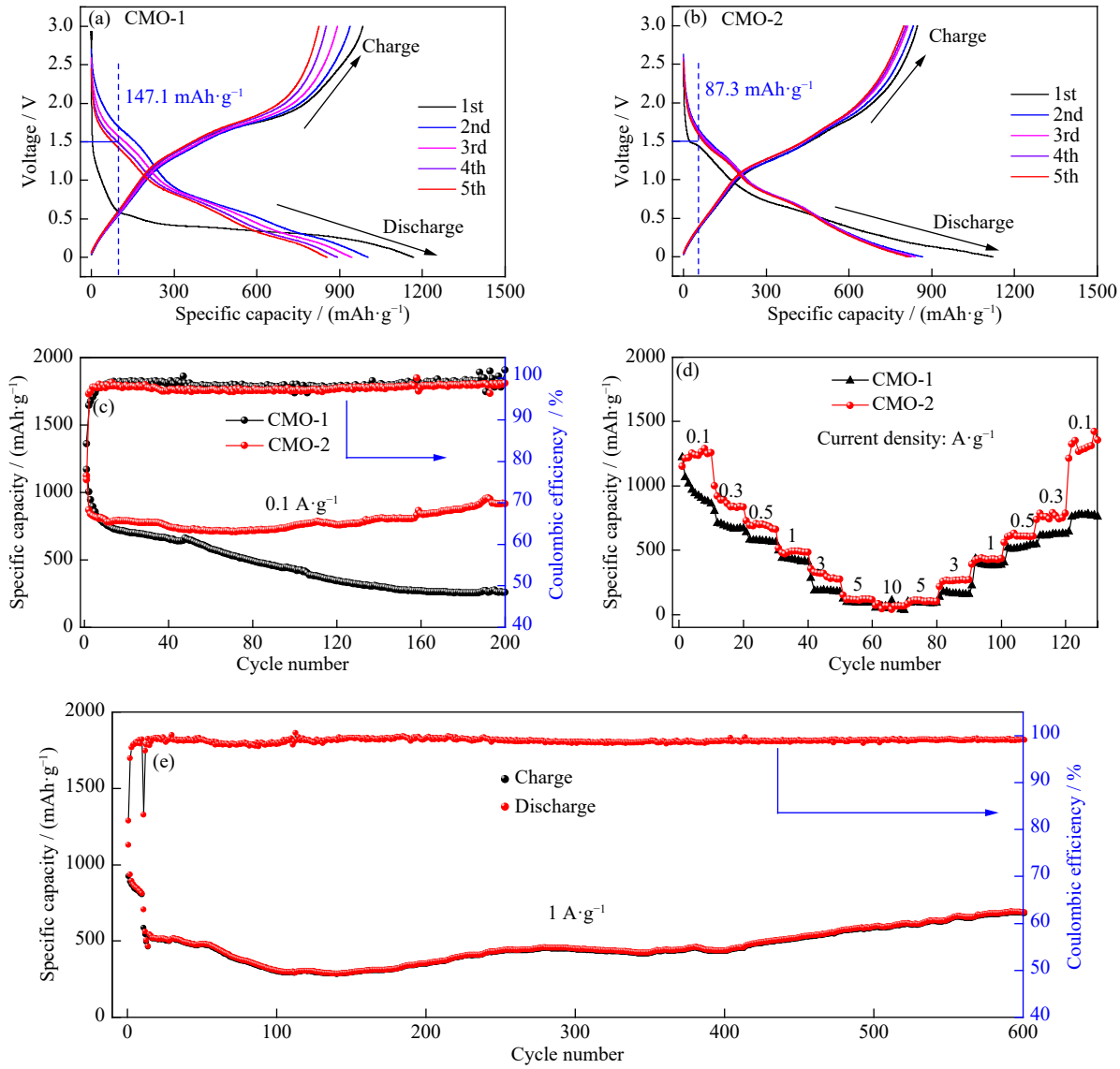

Fig. 4. (a, b) CV discharge/charge profiles of CMO-1 and CMO-2, respectively; (c) cycling performancesat 0.1 A/g and (d) rate performances of CMO-1 and CMO-2; (e) prolonged cycling performance of CMO-2 at 1 A/g.

Fig. 4(c) depicts the cycling performances of CMO-1 and CMO-2 at 0.1 A/g after 200 cycles. Upon initial discharge, CMO-1 delivered a specific capacity of 1168.2 mAh/g, surpassing that of CMO-2 (1122.0 mAh/g). However, an evident capacity fade was observed during cycling, which resulted in a high-capacity loss of up to 77.81% for CMO-1 after 200 cycles. The capacity retention of CMO-2 after 200 cycles reached 81.69%, which is considerably higher than that of CMO-1. The result signifies that the better cycling stability of CMO-2 was due to the introduction of highly active nanosized $CoMoO_3$ into $CoMoO_4$, which not only promoted the fully reversible conversion in $CoMoO_4$ but also provided a better cushion to accommodate volumetric swelling during cycling. Moreover, the capacity of CMO-2 continuously increased after approximately 80 cycles due to the activation of additional active material surfaces and the improved electrochemical reactions during the cycling process, consistent with the observation in a similar study [52].

Fig. 4(d) illustrates the rate performances of CMO-1 and CMO-2. At various current densities, CMO-2 delivered dis-

charge specific capacities of 1257.8, 832.4, 660.1, 484.1, 273.6, 115.3, and 63.9 mAh/g at 0.1, 0.3, 0.5, 1, 3, 5, and 10 A/g, respectively. Conversely, CMO-1 exhibited a poorer rate capability, with capacities of 860.7, 669.8, 563.9, 409.4, 177.6, 98.6, and 53.6 mAh/g at the corresponding current densities. After cycling at various rates and the current density reverting to 0.1 A/g, CMO-1 and CMO-2 recovered to 760.3 and 1355.9 mAh/g, respectively, which implies that the electrodes maintained their structural robustness at elevated current densities. Furthermore, the long cycling stability of CMO-2 was investigated. Fig. 4(e) shows its substantial capacity of 683.4 mAh/g after 600 cycles at 1 A/g, which proves its excellent cycling stability.

3.2. Discussion

To explore the mechanism accounting for their improved electrochemical performance, CMO-1 and CMO-2 were subjected to CV measurements at different scan rates (Fig. 5(a) and (b)). The stored charge within the electrode is chiefly derived from two processes, namely, (i) faradaic intercalation and (ii) capacitive processes, which is related to the faradaic charge transfer at/near the surface. Qualitative analysis of the capacitive contribution to capacity was performed referring to the following equation [53–57]:

$$i = av^b \tag{1}$$

Eq. (1) is reformatted to Eq. (2):

$$\lg i = \lg a + b\lg v \tag{2}$$

where v signifies the scan rate, i denotes the current at a consistent potential, and the equation features a and b are tunable parameters. b value was identified from the slope of lg$a$ versus lg$v$, a key indicator of charge storage kinetics. For the process controlled by diffusion (faradaic process), b was close to 0.5, whereas for processes dominated by capacitive

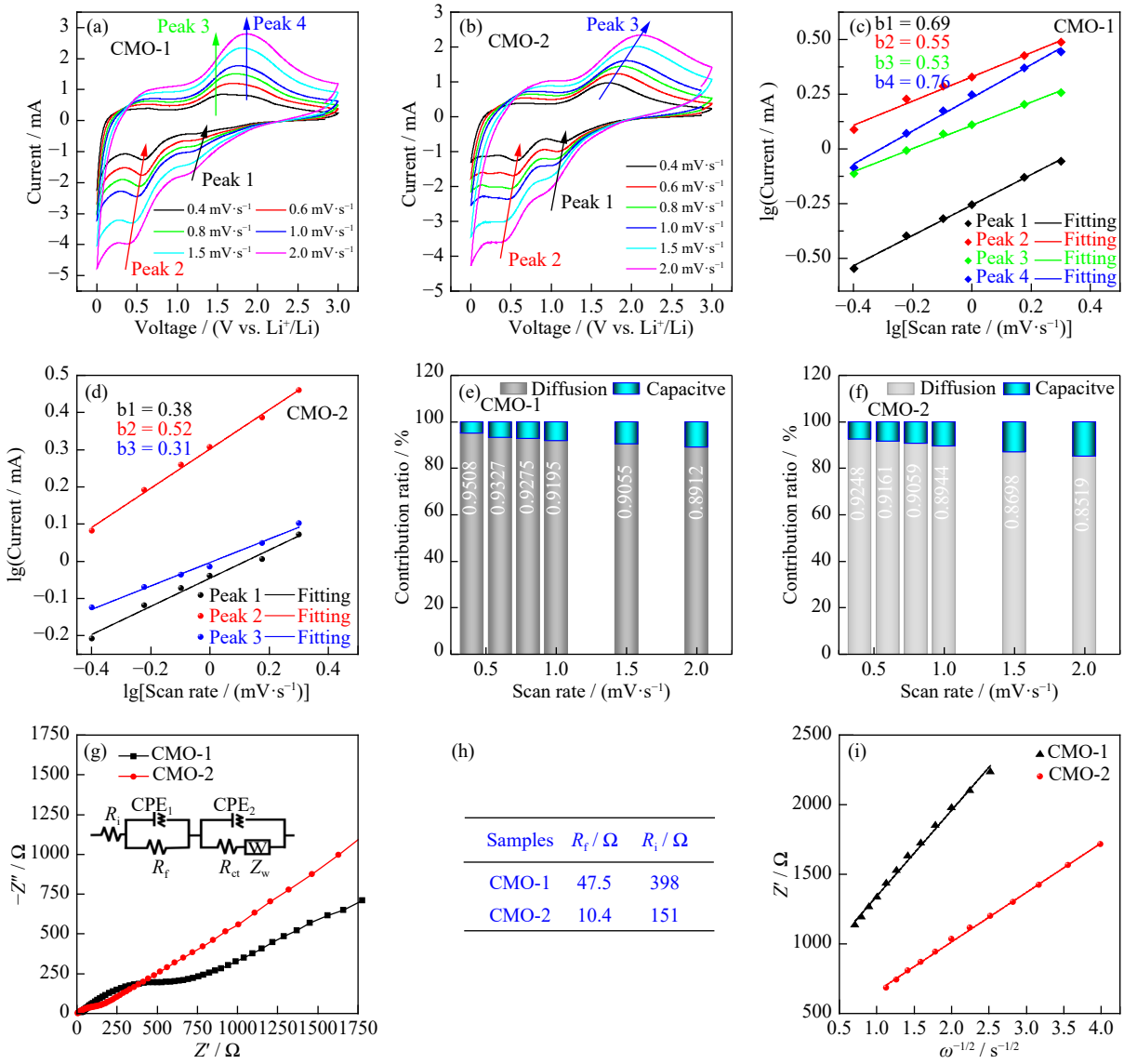

Samples	R_f / Ω	R_s / Ω
CMO-1	47.5	398
CMO-2	10.4	151

Fig. 5. CV profiles of (a) CMO-1 and (b) CMO-2 at varying scan rates from 0.4 to 2 mV/s; lg$i$ vs. lg$v$ curves of (c) CMO-1 and (d) CMO-2; capacitive and diffusion-controlled process ratios of (e) CMO-1 and (f) CMO-2 at different scan speeds; (g) Nyquist profiles and (h) fitting results of the EIS data of CMO-1 and CMO-2 at 0.1 A/g after 200 cycles; (i) corresponding Z'–$\omega^{-1/2}$ plots of CMO-1 and CMO-2.

behavior, its value was close to 1. Parameter b was calculated using the peaks marked in Fig. 5(a) and (b). The corresponding values were 0.69 (peak 1), 0.55 (peak 2), 0.53 (peak 3), and 0.76 (peak 4) for CMO-1 (Fig. 5(c)) and 0.38 (peak 1), 0.52 (peak 2), and 0.31 (peak 3) for CMO-2 (Fig. 5(d)). Values clustering around 0.5 indicated a dominant diffusion contribution to charge storage. This outcome verifies that the lithium-storage mechanism of CMO-1 and CMO-2 depends on conversion reactions.

The relative dominance of capacitive and diffusion-controlled processes for CMO-1 and CMO-2 can be determined using the following equations [53–54,58–63]:

$$i(\mathrm{V}) = k_1 v + k_2 v^{1/2} \tag{3}$$

Eq. (3) is reformatted to Eq. (4):

$$i(V)/v^{0.5} = k_1 v^{0.5} + k_2 \tag{4}$$

where k_1 and k_2 denote the coefficients for surface-capacitive and diffusion-controlled processes, respectively; i(V) denotes the current at a fix potential. Both constants are defined in Eq. (4) and can be evaluated accordingly. Fig. 5(e) and (f) provides a visual representation of the calculated contributions from the diffusion-controlled and capacitive processes of CMO-1 and CMO-2 at different scan rates, respectively. With the increase in the scan rate, the capacitive contributions of CMO-1 and CMO-2 ascended to 10.88% and 14.81% (at 2 mV/s), respectively, from the initial values of 4.92% and 7.52% (at 0.4 mV/s). CMO-2 exhibited higher capacitive contributions than CMO-1 at each scan rate.

EIS measurement proved vital to the evaluation of the improved performance of the samples. Fig. S2(a) and (b) shows the Nyquist plots of CMO-1 and CMO-2, respectively, with the same discharge state from 308.15 to 388.15 K. The plots share three distinctive components: (I) a minor depressed semicircle at high frequencies, which is associated with the SEI film resistance (R_f) and constant phase element (CPE1); (II) a depressed arc at the intermediate frequency range, which stemmed from the resistance to R_{ct} (electron transfer) and CPE2; (III) a straight-line feature in the low-frequency range, which points to the Warburg impedance (Z_w) associated with Li^+ migration. To further clarify the effect of introducing $CoMoO_3$ into $CoMoO_4$ on the activation energy of the interfacial reaction, the corresponding activation energy (E_a) for the samples was calculated through the following modified Butler–Volmer equation [64]:

$$\frac{T}{R_{ct}} = A\exp\left(-\frac{E_a}{RT}\right) \tag{5}$$

Eq. (5) was reformatted to Eq. (6):

$$\lg\frac{T}{R_{ct}} = -\frac{E_a}{2.303R}\times\frac{1000}{T} \tag{6}$$

where A is the pre-exponential factor, T is the absolute temperature, R is 8.314 $J\cdot mol^{-1}\cdot K^{-1}$, and $-\frac{E_a}{2.303R}$ was identified from the slope of $\lg\frac{T}{R_{ct}}$ versus $\frac{1000}{T}$. The corresponding values were −1.83 for CMO-1 (Fig. S2(c)) and −0.42 for CMO-2 (Fig. S2(d)), and the E_a values of CMO-1 and CMO-2 were 35.04 and 8.06 kJ/mol, respectively. The results indicate that the charge transfer interfacial reaction of CMO-2 was more readily conducted, which exhibited excellent reversible and rate performances than CMO-1. Fig. 5(g) shows the Nyquist plots of CMO-1 and CMO-2 after cycling for 200 cycles at 0.1 A/g. As shown in Fig. 5(h), CMO-2 exhibited a better charge transfer ability than CMO-1. To further clarify the effect of introducing $CoMoO_3$ into $CoMoO_4$ on the lithium-ion diffusion, the corresponding ion diffusion coefficients (D_{Li^+}) for the CMO-1 and CMO-2 samples were calculated using the following equation [65–66]:

$$D_{Li^+} = 0.5\times\frac{R^2T^2}{S^2n^4F^4C_{Li^+}^2\sigma^2} \tag{7}$$

where T equals 2981.5 K, S is the electrode area (1.54 cm^2), n signifies the number of transferred electrons involved in the electrochemical redox reaction (8), F is 96500 C/mol (Faraday's constant), C_{Li^+} indicates the molar concentration of Li^+ in the solid (3.56×10^{-5} $mol\cdot cm^{-3}$), and σ was calculated by evaluating the slope of the Z'–$\omega^{-1/2}$ line segments (Fig. 5(i)), with values of 617.5 and 355.3 $rad^{1/2}\cdot s^{1/2}$ for CMO-1 and CMO-2, respectively. Therefore, the D_{Li^+} values were calculated using Eq. (7). The D_{Li^+} for CMO-2 was 1.74 times higher than that of CMO-1, which implies that the introduction of $CoMoO_3$ into $CoMoO_4$ can facilitate ion diffusion in the electrode.

Furthermore, to highlight the outstanding reversibility performance for LIBs, Table S2 demonstrated the comparison of CMO-2 and other reported $CoMoO_4$-based electrodes. Evidently, the lithium-storage performance of CMO-2, particularly for long-term cycling performance, is as good as or better than that of $CoMoO_4$ with various amorphous or carbon coatings. In addition, CMO-2 showed a reversible lithium-storage capacity similar to the benefits observed with the incorporation of Co_3O_4 into $CoMoO_4$. The above characterizations and analyses revealed that the remarkable lithium-storage performance of CMO-2 was due to the following: (i) high specific surface area supplied ample active sites for ion hosting; (ii) low R_{ct} promoted optimal charge transfer during the discharge/charge process; (iii) the introduction of $CoMoO_3$ into $CoMoO_4$ can effectively decrease the activation energy of the interfacial reaction, which promotes Li^+ diffusion and storage.

4. Conclusion

CMO-2 nanorods have been successfully synthesized by employing a simple solvo-hydrothermal approach, followed by an annealing approach to finalize the structure. Introducing $CoMoO_3$ into $CoMoO_4$ can boost charge transfer efficiency at the electrode contact and promote the rapid movement of Li^+ within the electrode. In addition, nanorod structure can reduce the distance that ions must travel, which facilitates the process of Li^+ insertion and extraction. Therefore, CMO-2 exhibited excellent lithium-storage performance, including specific capacity and cycling stability (919.6 mAh/g at 0.1 A/g after 200 cycles and 683.4 mAh/g at 1 A/g after

600 cycles). The strategy presented in this work will serve as a promising means to promote the development of highly reversible capacity metal oxides for high-performance LIBs.

Acknowledgements

This work was supported by Jiangxi Provincial Natural Science Foundation, China (Nos. 20242BAB25195 and 20224BAB211018), National Natural Science Foundation of China (No. 12264029), the Scientific Research Foundation of Jiangxi Provincial Education Department, China (No. GJJ211944), and the college Students' Innovation and Entrepreneurship Training program of Jiangxi Province, China.

Conflicts of Interest

The authors declare that there is no conflict of financial or non-financial interests related to this article.

Supplementary Information

The online version contains supplementary material available at https://doi.org/10.1007/s12613-024-3051-0.

References

[1] P. Poizot, S. Laruelle, S. Grugeon, L. Dupont, and J.M. Tarascon, Nano-sized transition-metal oxides as negative-electrode materials for lithium-ion batteries, *Nature*, 407(2000), No. 6803, p. 496.

[2] Y. Lu, L. Yu, and X.W. Lou, Nanostructured conversion-type anode materials for advanced lithium-ion batteries, *Chem*, 4(2018), No. 5, p. 972.

[3] G.S. Xu, M.X. Jiang, J.L. Li, *et al*., Machine learning-accelerated discovery and design of electrode materials and electrolytes for lithium ion batteries, *Energy Storage Mater.*, 72(2024), art. No. 103710.

[4] S.H. Yu, S.H. Lee, D.J. Lee, Y.E. Sung, and T. Hyeon, Conversion reaction-based oxide nanomaterials for lithium ion battery anodes, *Small*, 12(2016), No. 16, p. 2146.

[5] D. Zhang, C.Y. Zhang, X. Zheng, *et al*., Facile synthesis of the Mn_3O_4 polyhedron grown on N-doped honeycomb carbon as high-performance negative material for lithium-ion batteries, *Int. J. Miner. Metall. Mater.*, 30(2023), No. 6, p. 1152.

[6] M. Ebner, F. Marone, M. Stampanoni, and V. Wood, Visualization and quantification of electrochemical and mechanical degradation in Li ion batteries, *Science*, 342(2013), No. 6159, p. 716.

[7] K.H. Seng, M.H. Park, Z.P. Guo, H.K. Liu, and J. Cho, Catalytic role of Ge in highly reversible GeO_2/Ge/C nanocomposite anode material for lithium batteries, *Nano Lett.*, 13(2013), No. 3, p. 1230.

[8] Z.H. Yang, C.C. Weng, X.Y. Gao, *et al*., *In situ* construction of Sn-based metal–organic frameworks on MXene achieving fast electron transfer for rapid lithium storage, *Chem. Eng. J.*, 486(2024), art. No. 150299.

[9] K.Z. Cao, S.T. Wang, Y.N. He, J.H. Ma, Z.W. Yue, and H.Q. Liu, Constructing Al@C–Sn pellet anode without passivation layer for lithium-ion battery, *Int. J. Miner. Metall. Mater.*, 31(2024), No. 3, p. 552.

[10] D.H. Wang, R. Kou, D. Choi, *et al*., Ternary self-assembly of ordered metal oxide–graphene nanocomposites for electrochemical energy storage, *ACS Nano*, 4(2010), No. 3, p. 1587.

[11] J. Yu, Y.L. Wang, L.H. Mou, D.L. Fang, S.M. Chen, and S.J. Zhang, Nature-inspired 2D-mosaic 3D-gradient mesoporous framework: Bimetal oxide dual-composite strategy toward ultrastable and high-capacity lithium storage, *ACS Nano*, 12(2018), No. 2, p. 2035.

[12] X.Y. Hou, S. Xue, M.T. Liu, X.N. Shang, Y.J. Fu, and D.Y. He, Hollow irregular octahedra-like $NiCo_2O_4$ cages composed of mesoporous nanosheets as a superior anode material for lithium-ion batteries, *Chem. Eng. J.*, 350(2018), p. 29.

[13] J.F. Li, L. Han, X.J. Zhang, *et al*., Sb_2O_5/Co-containing carbon polyhedra as anode material for high-performance lithium-ion batteries, *Chem. Eng. J.*, 370(2019), p. 800.

[14] N.N. Leyzerovich, K.G. Bramnik, T. Buhrmester, H. Ehrenberg, and H. Fuess, Electrochemical intercalation of lithium in ternary metal molybdates $MMoO_4$ (M: Cu, Zn, Ni and Fe), *J. Power Sources*, 127(2004), No. 1-2, p. 76.

[15] H. Yu, C. Guan, X.H. Rui, *et al*., Hierarchically porous three-dimensional electrodes of $CoMoO_4$ and $ZnCo_2O_4$ and their high anode performance for lithium ion batteries, *Nanoscale*, 6(2014), No. 18, p. 10556.

[16] C.C. Weng, S.M. Huang, T. Lu, *et al*., NiM (Sb, Sn)/N-doped hollow carbon tube as high-rate and high-capacity anode for lithium-ion batteries, *J. Colloid Interface Sci.*, 652(2023), p. 208.

[17] W. Xiao, J.S. Chen, C.M. Li, R. Xu, and X.W. Lou, Synthesis, characterization, and lithium storage capability of $AMoO_4$ (A = Ni, Co) nanorods, *Chem. Mater.*, 22(2010), No. 3, p. 746.

[18] J.B. Li, D. Yan, S.J. Hou, *et al*., Metal-organic frameworks derived yolk–shell ZnO/NiO microspheres as high-performance anode materials for lithium-ion batteries, *Chem. Eng. J.*, 335(2018), p. 579.

[19] K. Tang, S.A. Farooqi, X.F. Wang, and C.L. Yan, Recent progress on molybdenum oxides for rechargeable batteries, *ChemSusChem*, 12(2019), No. 4, p. 755.

[20] L.J. Wang, X.H. Cui, L.L. Gong, *et al*., Synthesis of porous $CoMoO_4$ nanorods as a bifunctional cathode catalyst for a Li–O_2 battery and superior anode for a Li-ion battery, *Nanoscale*, 9(2017), No. 11, p. 3898.

[21] J. Yu, Y.B. Wei, B.C. Meng, *et al*., Homogeneous distributed natural pyrite-derived composite induced by modified graphite as high-performance lithium-ion batteries anode, *Int. J. Miner. Metall. Mater.*, 30(2023), No. 7, p. 1353.

[22] Z.L. Li, Y.Z. Yang, J. Wang, Z. Yang, and H.L. Zhao, Sandwich-like structure C/SiO_x@graphene anode material with high electrochemical performance for lithium ion batteries, *Int. J. Miner. Metall. Mater.*, 29(2022), No. 11, p. 1947.

[23] Z.H. Zheng, M.Z. Xie, G.Q. Yu, *et al*., Preparation of lithium-ion battery anode materials from graphitized spent carbon cathode derived from aluminum electrolysis, *Int. J. Miner. Metall. Mater.*, 31(2024), No. 11, p. 2466.

[24] W.X. Liu, T. Xie, X.W. Wang, *et al*., Diffusion of carbon quantum dots on lithium liquid metal for artificial SEI, *Adv. Funct. Mater.*, 34(2024), No. 52, art. No. 2410843.

[25] Y.P. Chen, B.R. Liu, W. Jiang, *et al*., Coaxial three-dimensional $CoMoO_4$ nanowire arrays with conductive coating on carbon cloth for high-performance lithium ion battery anode, *J. Power Sources*, 300(2015), p. 132.

[26] J.Y. Yao, Y.J. Gong, S.B. Yang, *et al*., $CoMoO_4$ nanoparticles anchored on reduced graphene oxide nanocomposites as anodes for long-life lithium-ion batteries, *ACS Appl. Mater. Interfaces*, 6(2014), No. 22, p. 20414.

[27] Y.L. Zhu, Y.X. Wang, C. Gao, W.N. Zhao, X.B. Wang, and M.B. Wu, $CoMoO_4$–N-doped carbon hybrid nanoparticles loaded on a petroleum asphalt-based porous carbon for lithium storage, *New Carbon Mater.*, 35(2020), No. 4, p. 358.

[28] L.X. Li, G.S. Dong, H. Zhao, *et al*., Coral-like $CoMoO_4$ hierarchical structure uniformly encapsulated by graphene-like N-doped carbon network as an anode for high-performance lithium-ion batteries, *J. Colloid Interface Sci.*, 586(2021), p. 11.

[29] Y. Xiao, J.Y. Hwang, and Y.K. Sun, Micro-intertexture carbon-free iron sulfides as advanced high tap density anodes for rechargeable batteries, *ACS Appl. Mater. Interfaces*, 9(2017), No. 45, p. 39416.

[30] W. Wang, J.W. Qin, Z.G. Yin, and M.H. Cao, Achieving fully reversible conversion in MoO_3 for lithium ion batteries by rational introduction of $CoMoO_4$, *ACS Nano*, 10(2016), No. 11, p. 10106.

[31] Y.Y. Chen, Y. Wang, X.P. Shen, *et al*., Cyanide–metal framework derived $CoMoO_4/Co_3O_4$ hollow porous octahedrons as advanced anodes for high performance lithium ion batteries, *J. Mater. Chem. A*, 6(2018), No. 3, p. 1048.

[32] M.X. Jiang, Y.J. Zhang, Z.H. Yang, *et al*., A data-driven interpretable method to predict capacities of metal ion doped TiO_2 anode materials for lithium-ion batteries using machine learning classifiers, *Inorg. Chem. Front.*, 10(2023), No. 22, p. 6646.

[33] C.C. Weng, L. Ma, B.F. Wang, *et al*., Single-solvent ionic liquid strategy achieving wide-temperature and ultra-high cut-off voltage for lithium metal batteries, *Energy Storage Mater.*, 71(2024), art. No. 103584.

[34] J. Chen, A.M. Rao, C.T. Gao, *et al*., Phase-transition-free rivets for layered oxide potassium cathodes, *Nano Res.*, 17(2024), No. 11, p. 9671.

[35] J.K. Wang, T.H. Yao, L.L. Wang, Z.Y. Wang, Z.D. Wang, and H.K. Wang, Structural engineering of $CoMoO_3$ nanosheets on cage-like carbon nanoflakes toward enhanced lithium storage performance, *J. Alloy. Compd.*, 926(2022), art. No. 166871.

[36] S.K. Marka, S. Petnikota, V.V.S.S. Srikanth, M.V. Reddy, S. Adams, and B.V.R. Chowdari, $Co_2Mo_3O_8$/reduced graphene oxide composite: Synthesis, characterization, and its role as a prospective anode material in lithium ion batteries, *RSC Adv.*, 6(2016), No. 60, p. 55167.

[37] L.F. Xie, T. Chen, H.C. Chan, Y.J. Shu, and Q.S. Gao, Hydrogen doping into MoO_3 supports toward modulated metal-support interactions and efficient furfural hydrogenation on iridium nanocatalysts, *Chem. Asian J.*, 13(2018), No. 6, p. 641.

[38] Z. Liu, C.H. Zhan, L.K. Peng, *et al*., A $CoMoO_4$–$Co_2Mo_3O_8$ heterostructure with valence-rich molybdenum for a high-performance hydrogen evolution reaction in alkaline solution, *J. Mater. Chem. A*, 7(2019), No. 28, p. 16761.

[39] G.W. Smith and J.A. Ibers, The crystal structure of cobalt molybdate $CoMoO_4$, *Acta Crystallogr.*, 19(1965), No. 2, p. 269.

[40] L. Lei, L.M. Fang, L.F. Zhai, R. Wang, and M. Sun, Anodic oxidation-assisted O_2 oxidation of phenol catalyzed by Fe_3O_4 at low voltage, *Electrochim. Acta*, 261(2018), p. 394.

[41] J.A. Rodriguez, J.Y. Kim, J.C. Hanson, and J.L. Brito, Reduction of $CoMoO_4$ and $NiMoO_4$: *In situ* time-resolved XRD studies, *Catal. Lett.*, 82 (2002), No. 1, p. 103.

[42] M. Li, S.H. Xu, C. Cherry, *et al*., Hierarchical 3-dimensional $CoMoO_4$ nanoflakes on a macroporous electrically conductive network with superior electrochemical performance, *J. Mater. Chem. A*, 3(2015), No. 26, p. 13776.

[43] S. Baskar, D. Meyrick, K.S. Ramakrishnan, and M. Minakshi, Facile and large scale combustion synthesis of α-$CoMoO_4$: Mimics the redox behavior of a battery in aqueous hybrid device, *Chem. Eng. J.*, 253(2014), p. 502.

[44] J. Xu, S.Z. Gu, L. Fan, P. Xu, and B.G. Lu, Electrospun lotus root-like $CoMoO_4$@graphene nanofibers as high-performance anode for lithium ion batteries, *Electrochim. Acta*, 196(2016), p. 125.

[45] D.T. Dam, T. Huang, and J.M. Lee, Ultra-small and low crystalline $CoMoO_4$ nanorods for electrochemical capacitors, *Sustainable Energy Fuels*, 1(2017), No. 2, p. 324.

[46] R. Xu, J.M. Lin, J.H. Wu, *et al*., Hydrothermal synthesis of $CoMoO_4/Co_9S_8$ nanorod arrays on nickel foam for high-performance asymmetric supercapacitors with high energy density, *Electrochim. Acta*, 252(2017), p. 470.

[47] Y.Q. Ou, W.Q. Tian, L. Liu, Y.H. Zhang, and P. Xiao, Bimetallic $Co_2Mo_3O_8$ suboxides coupled with conductive cobalt nanowires for efficient and durable hydrogen evolution in alkaline electrolyte, *J. Mater. Chem. A*, 6(2018), No. 12, p. 5217.

[48] Y.Q. Li, H.B. Xu, H.Y. Huang, C. Wang, L.G. Gao, and T.L. Ma, One-dimensional MoO_2–$Co_2Mo_3O_8$@C nanorods: A novel and highly efficient oxygen evolution reaction catalyst derived from metal–organic framework composites, *Chem. Commun.*, 54(2018), No. 22, p. 2739.

[49] M.Q. Yu, L.X. Jiang, and H.G. Yang, Ultrathin nanosheets constructed $CoMoO_4$ porous flowers with high activity for electrocatalytic oxygen evolution, *Chem. Commun.*, 51(2015), No. 76, p. 14361.

[50] J.J. Jasieniak, N.D. Treat, C.R. McNeill, B.J.T. de Villers, E.D. Gaspera, and M.L. Chabinyc, Interfacial characteristics of efficient bulk heterojunction solar cells fabricated on MoO_x anode interlayers, *Adv. Mater.*, 28(2016), No. 20, p. 3944.

[51] C.T. Cherian, M.V. Reddy, S.C. Haur, and B.V.R. Chowdari, Interconnected network of $CoMoO_4$ submicrometer particles as high capacity anode material for lithium ion batteries, *ACS Appl. Mater. Interfaces*, 5(2013), No. 3, p. 918.

[52] X. Wu, X.Y. Xiong, B. Yuan, J. Liu, and R.Z. Hu, Understanding the phenomenon of capacity increasing along cycles: In the case of an ultralong-life and high-rate SnSe–Mo–C anode for lithium storage, *J. Energy Chem.*, 72(2022), p. 133.

[53] T. Brezesinski, J. Wang, S.H. Tolbert, and B. Dunn, Ordered mesoporous alpha-MoO_3 with iso-oriented nanocrystalline walls for thin-film pseudocapacitors, *Nat. Mater.*, 9(2010), No. 2, p. 146.

[54] V. Augustyn, J. Come, M.A. Lowe, *et al*., High-rate electrochemical energy storage through Li^+ intercalation pseudocapacitance, *Nat. Mater.*, 12(2013), No. 6, p. 518.

[55] J.B. Cook, H.S. Kim, Y. Yan, *et al*., Mesoporous MoS_2 as a transition metal dichalcogenide exhibiting pseudocapacitive Li and Na-ion charge storage, *Adv. Energy Mater.*, 6(2016), No. 9, art. No. 1501937.

[56] J.B. Li, D. Yan, S.J. Hou, T. Lu, Y.F. Yao, and L.K. Pan, Metal-organic frameworks converted flower-like hybrid with Co_3O_4 nanoparticles decorated on nitrogen-doped carbon sheets for boosted lithium storage performance, *Chem. Eng. J.*, 354(2018), p. 172.

[57] J.B. Li, Z.B. Ding, J.L. Li, C.Y. Wang, L.K. Pan, and G.X. Wang, Synergistic coupling of $NiS_{1.03}$ nanoparticle with S-doped reduced graphene oxide for enhanced lithium and sodium storage, *Chem. Eng. J.*, 407(2021), art. No. 127199.

[58] H.S. Kim, J.B. Cook, H. Lin, *et al*., Oxygen vacancies enhance pseudocapacitive charge storage properties of MoO_{3-x}, *Nat. Mater.*, 16(2017), No. 4, p. 454.

[59] M. Salanne, B. Rotenberg, K. Naoi, *et al*., Efficient storage mechanisms for building better supercapacitors, *Nat. Energy*, 1(2016), art. No. 16070.

[60] J.B. Li, D. Yan, S.J. Hou, *et al*., Improved sodium-ion storage performance of $Ti_3C_2T_x$ MXenes by sulfur doping, *J. Mater.*

Chem. A, 6(2018), No. 3, p. 1234.

[61] J.F. Li, L. Han, X.L. Zhang, *et al*., Multi-role TiO_2 layer coated carbon@few-layered MoS_2 nanotubes for durable lithium storage, *Chem. Eng. J.*, 406(2021), art. No. 126873.

[62] J.B. Li, Z.B. Ding, L.K. Pan, J.L. Li, C.Y. Wang, and G.X. Wang, Facile self-templating synthesis of layered carbon with N, S dual doping for highly efficient sodium storage, *Carbon*, 173(2021), p. 31.

[63] H.P. Lei, T.W. Wei, J.G. Tu, and S.Q. Jiao, Core–shell mesoporous carbon hollow spheres as Se hosts for advanced Al–Se batteries, *Int. J. Miner. Metall. Mater.*, 31(2024), No. 5, p. 899.

[64] E.J.F. Dickinson and A.J. Wain, The Butler–Volmer equation in electrochemical theory: Origins, value, and practical application, *J. Electroanal. Chem.*, 872(2020), art. No. 114145.

[65] D. Yan, C.Y. Yu, X.J. Zhang, *et al*., Enhanced electrochemical performances of anatase TiO_2 nanotubes by synergetic doping of Ni and N for sodium-ion batteries, *Electrochim. Acta*, 254(2017), p. 130.

[66] J.B. Li, J.L. Li, D. Yan, *et al*., Design of pomegranate-like clusters with NiS_2 nanoparticles anchored on nitrogen-doped porous carbon for improved sodium ion storage performance, *J. Mater. Chem. A*, 6(2018), No. 15, p. 6595.